Dynamics in photosynthetic transient complexes studied by paramagnetic NMR spectroscopy

Scanu, S.

Chapter IV

Loss of electrostatic interactions causes increase of dynamics within the plastocyanin-cytochrome *f* complex

Abstract

The studies presented in Chapter III on the photosynthetic electron transfer complex formed by cytochrome *f* and plastocyanin from *Nostoc sp.* PCC 7119 revealed that both hydrophobic interactions and electrostatic interactions, play a role in the process of complex formation. To study the balance between these two types of interactions in the encounter state and the final complex, the interaction between plastocyanin from *Phormidium laminosum* and cytochrome *f* from *Nostoc* was investigated, using NMR spectroscopy and Monte Carlo docking computations. This plastocyanin is a natural variant of that from *Nostoc*, in which the net positive charge of the protein is reverted to negative. Cytochrome f has a highly negative charge, and thus it was expected that the electrostatic interactions become unfavorable. NMR titrations indicated that a complex with an affinity intermediate between those of the *Nostoc* and *Phormidium laminosum* complexes is still formed. The orientation of plastocyanin in the complex was determined using pseudocontact shifts, demonstrating that the hydrophobic patch is the main site of interaction on plastocyanin similar to the head-on orientation found for the *Phormidium* complex. However, the interaction in the cross complex is dependent on electrostatic interactions, contrary to the *Phormidium* complex. The negative charge of plastocyanin decreases, but not abolishes, the attraction to cytochrome *f*, resulting in the formation of a more diffuse encounter complex than *Nostoc*, as could be determined using paramagnetic relaxation spectroscopy. This work illustrates the subtle interplay of electrostatic and hydrophobic interactions in complex formation of transient protein complexes. The results are discussed in the context of a model for complex formation on the basis of hydrophobic contacts in the encounter state.

Introduction

Protein association involves the formation of a dynamic encounter complex that is in equilibrium with the final, single-orientation complex.[1] In the encounter state, the proteins sample the surface of the partner, thus reducing the dimensionality of the search for the specific binding site.[21] Protein complex formation has been commonly described with a general model, in which the formation of the encounter complex is dominated by long-range electrostatic interactions, whereas the final state is determined by short-range interactions.[22] However, theoretical staudies demonstrated that desolvation can be a dominant interaction in the process of complex formation for systems with weak charge complementarity.[139,167,170] Furthermore, partial desolvation of the binding interface was reported for some encounter complexes.[140,171] The recent characterization of the encounter state of cytochrome *f* (^{N}Cyt *f*) and plastocyanin (^{N}Pc) complex from the cyanobacteria *Nostoc* sp. PCC 7119 ($^{N\text{-}N}$complex) demonstrated experimentally that electrostatic interactions alone cannot describe the encounter complex, suggesting that hydrophobic interactions also contribute to its formation (Chapter III). In the proposed model, long-range electrostatics result in the preorientation of ^{N}Pc relative to ^{N}Cyt *f* and hydrophobic interactions stabilize the encounter complex by promoting the overlap of the extended non-polar surfaces of both proteins. ^{N}Pc can diffuse in the hydrophobic interface and smoothly reach orientations capable of ET. The identification of hydrophobic interactions in the encounter state contrasts the view in which short-range interactions occur only in the final complex.[21]

Pc and Cyt *f* are photosynthetic redox partners in oxygenic organisms, such as plants, green algae and cyanobacteria. Pc is a soluble electron carrier, which shuttles electrons from Cyt *f* of the cytochrome b_6f complex to photosystem I.[4,167,168] The association of Pc and Cyt *f* is on the border between electrostatic-assisted[23] and desolvation-mediated association,[169] therefore representing a good model to elucidate the balance between electrostatic and hydrophobic interactions in protein complex formation. *In vitro*, electrostatic interactions enable fast association[7,8,59,60,66,69] and non-polar interactions favour the stabilization of the complex to in an ET active conformation.[46,54,98] The characterization of Pc-Cyt *f* complexes from several organisms revealed that small differences in the electrostatic surface properties of the individual proteins strongly influence both the binding equilibrium and the final orientations of the complexes. Both in plants[46,62,172] and in the cyanobacteria *Nostoc*[98] and *Prochlorothrix hollandica*,[32] electrostatic interactions influence the final orientation of Pc with respect to Cyt *f* within the complex and tilt the long side of Pc towards the small domain of Cyt *f* in the so-called side-on orientation. The complex from the cyanobacterium *Phormidium laminosum* ($^{Ph\text{-}Ph}$complex) was found instead in the head-on orientation, in which solely the hydrophobic ET site represents the binding site.[54] Neutralization of charged residues on the surface of ^{Ph}Pc[7] and ^{N}Pc[8] has shown to have greater effect on the kinetics of the reaction than similar modifications on ^{Ph}Cyt *f*[69] and ^{N}Cyt *f*,[66] respectively. ^{Ph}Cyt *f* and ^{N}Cyt *f* are electrostatically similar, with an overall charge of -13 and -15,[49] respectively, and a rather even distribution of the negative charges over the surfaces. The two Pcs

show 63% of amino acid sequence identity and very similar three-dimensional structures, but they vary considerably in their electrostatic properties. ^{N}Pc is overall positively charged with six lysines (K6, K11, K20, K24, K35 and K100) forming an extended charged patch, which juxtaposes the long side of ^{N}Cyt *f* in the side-on orientation. In ^{Ph}Pc, K11 and K20 are substituted by serine and asparagine, respectively, and the positively charged patch is composed by four lysines (K6, K30, K35 and K100), yielding a protein with a net negative charge (-1 at pH 6). To evaluate the effects that these electrostatic differences between the two Pcs can cause along the association pathway of Cyt *f* and Pc, the complex of ^{N}Cyt *f* and Zn-substituted ^{Ph}Pc ($^{N\text{-}Ph}$complex) was studied using NMR spectroscopy and computational approaches. The consequences of this on binding affinity, final complex orientation and encounter complex will be discussed in the light of the findings for the $^{N\text{-}N}$complex presented in Chapter III.

Experimental section

Protein production and purification

The plasmid pET11PC,[172] which contains the gene for wild type ^{Ph}Pc, was transformed in *E.coli* BL21 pLysS. ^{15}N enriched-Zn substituted Pc was produced as described before for ^{N}Pc,[29] with the difference that ampicilline (100 mg/L) and chloramphenicol (20 mg/L) were added to the growth media in stead of kanamycin (25 mg/L). The purification procedure was reported before.[54] The concentration of the protein was determined by absorbance spectroscopy using ε_{280} = 5 mM^{-1}cm^{-1}. The yield of pure protein was 4 mg/L of culture.
The pEAF-WT plasmid, containing the gene of the soluble domain (residue 1-254) of *Nostoc* sp. PCC7119 Cyf *f* was kindly provided by Prof. Dr. Miguel A. De la Rosa (University of Seville). Cyt *f* mutants were obtained using pEAF-WT plasmid as template for mutagenesis as described before (Chapter III).[29,143] Production and purification of the protein, and spin label attachment were performed as previously reported (Chapter III).[8,29]

NMR experiments

All NMR samples contained MES (20 mM, pH 6) and 6% D_2O for lock. The pH of the sample was adjusted with small aliquots of HCl (0.5 M) and NaOH (0.5 M). For the chemical shift perturbation (CSP) experiments Cyt *f* was titrated into Zn-substituted ^{15}N Pc (40 μM). Spectra were recorded at multiple Cyt *f*:Pc molar ratios (0.1, 0.2, 0.4, 0.6, 0.8, 1.0, 2.5, 5.0, 7.5, 10). For measurements of the PCSs, HSQC spectra of the free Pc and in the presence of ferric and ferrous Cyt *f* were acquired on the same sample. Ferric Cyt *f* was oxidized with $K_3[Fe(CN)_6]$ and loaded onto a PD10 column to remove the oxidant, concentrated and then added to Pc (final concentration 135μ M) to Cyt *f*:Pc molar ratio 3:1. Ferric Cyt *f* was then reduced by adding 10 molar equivalents of ascorbic acid directly into the sample. For the PRE experiments the ferric state of Cyt *f* was preserved by addition of $K_3[Fe(CN)_6]$

(50 μM). These samples contained 135 μM Cyt *f* for Q125C mutant and 300 μM for the other mutants, labelled with either MTS or MTSL. Samples also contained Zn-substituted ^{15}N Pc, 45 μM in the complex with Q125C Cyt *f* and 100 μM for the other Cyt *f* mutants. All NMR spectra were recorded at 298 K on a Bruker Avance III 600 MHz spectrometer equipped with a TCI-Z-GRAD CryoProbe. The ^{1}H-^{15}N HSQC spectra were acquired with 1024 and 80 complex points in the direct and indirect dimensions, respectively.

NMR data analysis

The NMR spectra were processed with NmrPipe[145] and analyzed with CcpNMR Analysis.[146] CSP analysis was carried out as described before.[29] PCS was defined as the chemical shift difference for a resonance in the presence of paramagnetic and diamagnetic Cyt *f*, according to previously reported procedures.[46,98]
The PREs were determined according to the procedure described by Battiste and Wagner.[81] The intensity ratio I_p/I_d of the Pc resonances in the presence of MTSL-Cyt *f* (I_p) and MTS-Cyt *f* (I_d) were normalized by dividing them by the average value of the ten largest I_p/I_d values (1.09 for Q7C, 1.05 for Q38C, 2.21 for N71C, 1.41 for Q125C, 1.16 for S181C and 1.25 for S192). The PRE (Γ_2) values were calculated according to Equation 4.1:

$$\frac{I_p}{I_d} = \frac{R_{2d}\exp\left(-\Gamma_2 t\right)}{R_{2d}+\Gamma_2} \qquad (4.1)$$

R_{2d} represents the transverse relaxation rate in the diamagnetic sample, which was calculated from the linewidth at half height obtained from a Lorentzian peak fit in the direct dimension, by using FUDA (this software was kindly provided by Dr. D. Fleming Hansen, University College London). The symbol *t* indicates the time for transverse relaxation during the pulse sequence (9 ms). The Γ_2 values were extrapolated to the 100% bound state using the experimentally obtained K_D. The uncertainty for I_p/I_d ratios ($\Delta\sigma_{Ip/Id}$) was determined by error propagation according to Equation 4.2:

$$\Delta\sigma_{\frac{I_p}{I_d}} = \frac{I_p}{I_d}\sqrt{\left(\frac{\sigma_p}{I_p}\right)^2+\left(\frac{\sigma_d}{I_d}\right)^2} \qquad (4.2)$$

In which σ_p and σ_d represent the noise level of paramagnetic and diamagnetic spectra, respectively. The noise level of each spectrum is represented by the standard deviation of the intensities measured at ten randomly chosen positions between the resonances.

Docking calculations

The structure of the soluble part of Cyt *f* (residues 1-254) used for the calculation was taken from PDB entry 2ZT9[147] as described before.[29] The structure of ^{Ph}Pc was

taken from PDB entry 2Q5B. The orientation of ^{Ph}Pc in complex with ^{N}Cyt *f* was determined by rigid body docking using solely PCS restraints with the option PARAstraints[174] in Xplor-NIH 2.9.9.[175] For this reason the observed $^{1}H\Delta\delta_{PCS}$ were extrapolated to 100% bound Pc by dividing them by the fraction bound (0.47). The size of the axial magnetic component of the magnetic susceptibility anisotropy tensor ($\Delta\chi_{ax}$), was derived from the g-tensor values measured by EPR spectroscopy on plant Cyt *f* (7×10^{-32} m^3).[98] However, the value required to obtain convergence of the structure calculations is much smaller. One reason for this is the temperature difference between the EPR measurements (10 K) and NMR spectra (taken at 298 K). The second reason is averaging effect occurring in the encounter state, which reduces the PCS considerably. The $\Delta\chi_{ax}$ was varied from 0.61 to 3.3×10^{-32} m^3. The best convergence was found for $\Delta\chi_{ax} = 0.87 \times 10^{-32}$ m^3, whereas it was taken to be 7×10^{-32} m^3 in the $^{N\text{-}N}$complex.[98] The intermolecular PCSs from the ferric haem iron of Cyt *f* to the backbone amide atoms in Pc were back calculated from the best 20 structures and compared with the experimental PCSs. Equation 4.3 was used for the PCSs calculation, assuming an axial magnetic susceptibility tensor oriented along the vector defined by the iron and the N-atom of Y1 of Cyt *f*:[46]

$$\Delta\delta_{PCS} = \frac{\Delta\chi_{ax}}{12\pi r^3}\left(3\cos^2\theta - 1\right) \quad (4.3)$$

In which $\Delta\delta_{PCS}$ is the PCS, r is the distance between haem iron and observed Pc nucleus, and θ is the angle between Pc nucleus, haem iron and the nitrogen of the amine group of Y1 in Cyt *f*. The $\Delta\chi_{ax}$ was also varied in the backcalculation of the PCSs, and the best fit between the average back calculated PCSs from the best 20 structures representing the final complex model and the experimental data was found for $\Delta\chi_{ax} = 0.87 \times 10^{-32}$ m^3 as well. The degree of agreement between observed (PCS^{obs}) and calculated (PCS^{calc}) PCSs was determined by the PCS Q factor, defined as:

$$Q_{PCS} = \sqrt{\frac{\Sigma\left(PCS^{obs} - PCS^{calc}\right)^2}{\Sigma\left(\left|PCS^{obs}\right| + \left|PCS^{calc}\right|\right)^2}} \quad (4.4)$$

The ensemble docking was performed as described for the $^{N\text{-}N}$complex (Chapter III). The restraints for the calculations were obtained according to Equation 4.5:

$$\Gamma_2^{obs} = f_1\Gamma_2^{ens} + f_2\Gamma_2^{final} \qquad f_1 + f_2 = 1 \quad (4.5)$$

The ensemble Γ_2 (Γ_2^{ens}) was calculated as the difference between observed Γ_2 (Γ_2^{obs}) and average back calculated Γ_2 from the model of the PCS-based final complex models (Γ_2^{final}). The calculations were carried out with f_2 values of = 0, 0.15, 0.25, 0.35, 0.5, 0.65, 0.75, 0.85, 0.95 and 1.0. The restraints were grouped into three classes as described before.[29] For the visualization of the encounter

complex ensemble 150 docking were performed, yielding 148 ensembles of seven Pc conformers, with a difference in the total restraint energy ≤20%.
The ensembles from separated dockings were evaluated by means of the averaged violation for all experimental restraints as described before (Chapter III). The intermolecular PCSs from the ferric haem iron of Cyt *f* to the backbone amide atoms of all Pc conformers (PCS^{ens}) were back calculated with Xplor NIH 2.9.9. PCS^{ens} were linearly combined with the back calculated PCSs from the final model (PCS^{final}) using different population fraction of the encounter complex (f_1) according to Equation 4.6:

$$PCS^{calc} = (1 - f_1)\, PCS^{single} + f_1\, PCS^{ens} \qquad (4.6)$$

The agreement between observed (PCS^{obs}) and calculated (PCS^{calc}) PCS was given by the PCS Q factor, as defined in equation 4.4.

Monte Carlo simulations of the encounter complex

The structure files for Cyt *f* and Pc were taken from the PDB entries 2ZT9[147] and 2Q5B, respectively. Monte Carlo simulations generate a Boltzmann distribution of encounter complexes according to their electrostatic-interaction energy.[57] The simulations were performed using a previously described approach (Chapter III).[28]

Results and discussion

Affinity and binding site

For the characterization of the non-physiological cyanobacterial $^{N\text{-}Ph}$complex formed by ^{N}Cyt *f* and ^{Ph}Pc, ^{15}N enriched Zn ^{Ph}Pc was titrated to either oxidized ^{N}Cyt *f* (Fe^{III}) or reduced ^{N}Cyt *f* (Fe^{II}) to molar ratios Pc:Cyt *f* 1:10 and 1:3, respectively. ^{Ph}Pc was produced with Zn rather than the Cu in the binding site to avoid the interference of ET and the disappearance of important resonances due to the line-broadening caused by the paramagnetic Cu.[155] Each titration point was monitored through the acquisition of ^{15}N-^{1}H HSQC spectra. Upon addition of Cyt *f* a number of resonances shifted in the spectrum, indicating complex formation. The appearance of shifting resonances indicates that free and bound Pc are in fast exchange on the NMR time scale. The binding curves for the most affected residues were obtained by plotting the CSP ($\Delta\delta_H$) versus Cyt *f*(Fe^{III})/Pc molar ratio, as shown in Figure 4.1A.

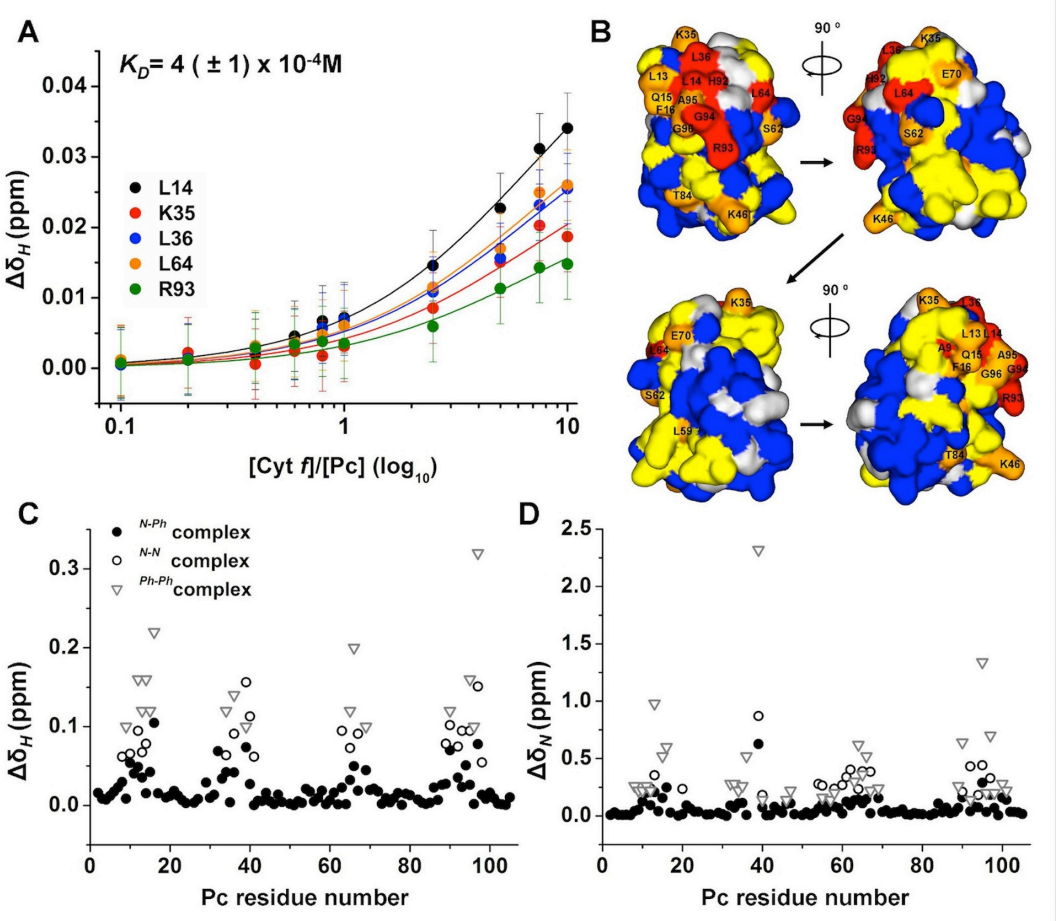

Figure 4.1. The interaction of Zn substituted ^{15}N ^{Ph}Pc with ^{N}Cyt *f*. A) CSP curves for Zn ^{Ph}Pc binding to ^{N}Cyt *f* for selected residues fitted to a 1:1 interaction model. B) Binding map of ^{Ph}Pc in the presence of wild type ^{N}Cyt *f* (Fe III), color-coded on a surface model of Pc (PDB entry 2Q5B). The red color corresponds to $\Delta\delta_{AVG} \geq$ 0.030 ppm, orange to $\Delta\delta_{AVG} \geq$ 0.015 ppm, yellow to $\Delta\delta_{AVG} \geq$ 0.0075 ppm, blue to $\Delta\delta_{AVG} \leq$ 0.0075 ppm. Prolines and overlapping residues are colored in light grey. (C, D) CSPs of ^{Ph}Pc resonances upon binding of ^{N}Cyt *f* (Fe II). The CSPs in ^{1}H dimension (C) and in ^{15}N dimension (D) observed for the $^{N\text{-}Ph}$complex are shown as black dots, for the $^{N\text{-}N}$complex as black circles and for $^{Ph\text{-}Ph}$complex as grey triangles.

The CSP curves did not reach saturation, indicating a low affinity. The global fit of the binding curves to a 1:1 binding model yielded a dissociation constant of 4 (± 1) × 10^{-4} M. This value is in between the reported values for the $^{Ph\text{-}Ph}$complex and $^{N\text{-}N}$complex, being ≈10 × 10^{-4} M[54] and 0.8 × 10^{-4} M,[29] respectively. Whereas the cross complex formed by ^{Ph}Cyt *f* and ^{N}Pc ($^{Ph\text{-}N}$complex) was reported to have similar affinity to $^{N\text{-}N}$complex (K_D= 0.8 × 10^{-4} M),[49] the $^{N\text{-}Ph}$complex shows an affinity intermediate to that of the two physiological complexes but closer to $^{Ph\text{-}Ph}$complex. The experimental K_D was used to determine that the fraction of ^{Ph}Pc bound to ^{N}Cyt *f* at the last point of the titration was 0.52 and the $\Delta\delta_{AVG}$ were extrapolated to the 100% bound form. The CSP map of Zn ^{Ph}Pc was obtained by color-coding each residue according to the size of $\Delta\delta_{AVG}$ (Figure 4.1B). The largest

effects were observed for residues surrounding the metal binding site, namely A9, L14, L36, H39, L64, H92, R93 and G94, colored in red. Most of these residues are hydrophobic and make up the hydrophobic patch of Pc, which was also identified as main binding site in the structural models of the $^{N\text{-}N}$complex and $^{Ph\text{-}Ph}$complex.[54,98] Clearly, the hydrophobic patch plays a fundamental role in the formation of the Cyt *f*-Pc complexes. The CSP map is qualitatively similar to that of the $^{N\text{-}N}$complex[29,98] with a prominent perturbation for R93, known to be involved in the binding in both the $^{N\text{-}N}$complex[8,66,98] and $^{Ph\text{-}Ph}$complex.[7] Interestingly, a significant CSP was also observed for K46 in the $^{N\text{-}Ph}$complex. K46 is located far from the hydrophobic patch, well below R93, and kinetic studies suggested its implication in the electrostatic modulation of the binding of $^{Ph\text{-}Ph}$complex.[67]

Structure of the final complex

The orientation of ^{Ph}Pc in complex with ^{N}Cyt *f* was determined by taking advantage of the intermolecular PCSs caused by the paramagnetic oxidized iron of Cyt *f* on Pc backbone amide protons, in a similar way as was done previously for other Pc-Cyt *f* complexes.[32,46,54,62] PCSs arise from the through-space dipolar interaction between the spin of the unpaired electron and that of the observed nucleus. PCS is distance and orientation dependent and provides restraints for structural calculations. The calculations converged to an ensemble of structures. The best 20 structures exhibit a difference in the restraint energy of less than 6% and are shown in Figure 4.2A.

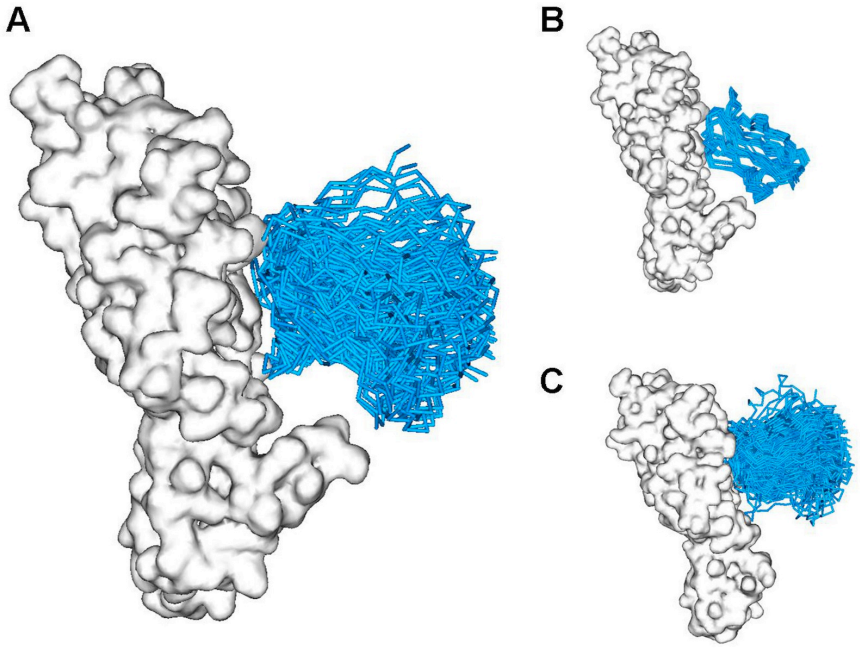

Figure 4.2. Comparison of the structures of Pc-Cyt *f* complexes, showing the structure obtained for the $^{N\text{-}Ph}$complex (A), and the physiological $^{N\text{-}N}$complex (PDB entry 1TU2[98]) (B) and $^{Ph\text{-}Ph}$complex (C). Cyt *f* is shown as a white surface model on the PDB entry 2ZT9 and Pc is represented by the ensemble of the 20 (A), 10 (B) and 25 (C) lowest energy conformations, shown as cyan C_α traces.

The resulting model shows a high degree of variability, but in all structures the hydrophobic patch of Pc is making contact with the hydrophobic patch surrounding the haem of Cyt *f* and represents the entire complex interface. All structures showed an interaction between H92 of Pc and F3 of Cyt *f*, also found in the *Ph-Ph*complex[54] and *N-N*complex.[98] The binding interface is composed of polar and hydrophobic residues, located in the regions 11-14, 36-39, 64-68 and 90-95 on *Ph*Pc. R93 represent the only charged interfacial residue. The averaged Cu-Fe distance in the ensemble was 15.3 (± 0.5) Å. In Figure 4.3A, the observed (black filled circles) and the back calculated PCSs for the best 20 structures (grey lines) are plotted versus Pc residue numbers.

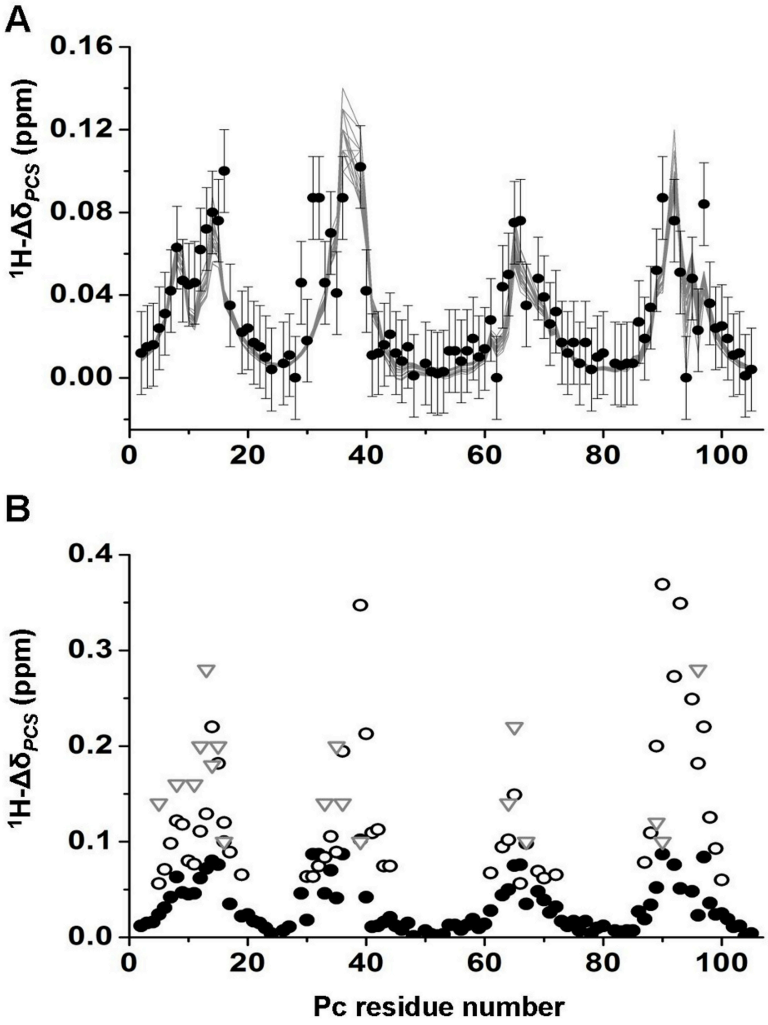

Figure 4.3. Evaluation of *N-Ph*complex. In panel A, the observed ^{1}HΔδ$_{PCS}$, which were extrapolated to 100% bound Pc, are shown as black filled circles and the back calculated ^{1}HΔδ$_{PCS}$ for the 20 lowest PCS energy structures are shown as grey lines. The error bars represent the estimated experimental errors in the resonance positions. In panel B, the observed ^{1}HΔδ$_{PCS}$ for the *N-Ph*complex are shown as black filled circles, for the *N-N*complex[98] as black open circles, and for the *Ph-Ph*complex[54] as grey triangles. All PCSs were extrapolated to the 100% bound form and plotted versus Pc residue numbers.

For most residues experimental and back calculated PCSs agree within the error margins. Small deviations are observed for F16, V29, W31, V32 and A90, which form the edge of the hydrophobic binding site, and M97, which coordinates the metal. Considering the relative vicinity of these residues to the haem, it is possible that the approximations made for the size, axiality and orientation of the magnetic susceptibility tensor cause these deviations. The overall quality of the structures was evaluated by calculating a quality (Q) factor for the back calculated PCSs for each structure of the final model and the experimental PCSs (See Experimental Section, Equation 4.4). The averaged Q value was calculated to be 0.23 (± 0.1).

The orientation of Pc in the complex is most similar to the head-on orientation found in the $^{Ph\text{-}Ph}$complex (Figure 4.2C) rather that the side-on orientation of the $^{N\text{-}N}$complex (Figure 4.2B). ^{Ph}Pc is oriented perpendicular to the haem with the hydrophobic patch at a slight angle to the small domain of ^{N}Cyt *f*. In the $^{N\text{-}N}$complex the specific electrostatic contacts between K57 and K62 of ^{N}Pc and E189 and D64 of ^{N}Cyt *f* appears to be responsible for the long side of Pc to be tilted toward Cyt *f*.[49,98] These lysines are substituted with D57 and S62, respectively, in ^{Ph}Pc and the loss of these important electrostatic contacts may lead to the "head-on" orientation in the $^{N\text{-}Ph}$complex. In the $^{N\text{-}Ph}$complex, only the bottom part of ^{Ph}Pc (relative to the hydrophobic patch) is turned toward the small domain of ^{N}Cyt *f*, probably as a consequence of the charge-charge interaction between K46 of ^{Ph}Pc and E189 and D190 of ^{N}Cyt *f*. The soluble part of ^{Ph}Cyt *f* is shorter than ^{N}Cyt *f*, comprizing 249 instead of 254 residues. This causes the small domain to be less extended and not in direct contact with Pc in the $^{Ph\text{-}Ph}$complex.[54] In the $^{N\text{-}Ph}$complex K46 is in a favorable position to have electrostatic interactions with E189 and D190 in the prominent small domain of Cyt *f*.

Since PCSs depend on the orientation of the observed nucleus with respect to the paramagnet, the presence of multiple orientations is expected to influence the size of PCSs. In Pc-Cyt *f* complex from *Prochlorothrix hollandica,* the mutation of Y12 and P14 in Pc to Gly and Leu, respectively, caused an increase of dynamics, as judged by the decrease of PCSs for nuclei in certain regions of Pc.[32] In Figure 3B, the observed $^{1}H\Delta\delta_{PCS}$ of $^{N\text{-}Ph}$complex were compared with the reported values for $^{N\text{-}N}$complex[98] and $^{Ph\text{-}Ph}$complex,[54] each extrapolated to the 100% bound state. The pattern of the $^{1}H\Delta\delta_{PCS}$ is similar for all complexes, but the sizes of $^{1}H\Delta\delta_{PCS}$ are comparable only for the two physiological complexes, whereas they are considerably lower for the $^{N\text{-}Ph}$complex. This indicates that in the $^{N\text{-}Ph}$complex the dynamics of Pc is larger than in both the $^{N\text{-}N}$complex and the $^{Ph\text{-}Ph}$complex.

The encounter complex

To map the distribution of the encounter intermediates on ^{N}Cyt *f* surface in the $^{N\text{-}Ph}$complex, six spin labels were attached on ^{N}Cyt *f*, one at a time, and PREs were measured on the amide backbone protons of ^{Ph}Pc. Cyt *f* was added to Pc in a molar ratio Pc:Cyt *f* of 1:3. PRE causes line broadening of Pc resonances resulting in a low ratio of peak intensities in the spectra of the paramagnetic and diamagnetic samples (I_p/I_d). In Figure 4.4 (*central panel*) the positions of spin labels are shown on a surface model of Cyt *f* with respect to Pc oriented as found

in the lowest energy structure of the PCS-based final complex (cyan C_α trace). Spin labels attached to Cyt *f* on the same side as the binding site for Pc, at positions Q7, N71, and S192, caused a large decrease of I_p/I_d ratios of Pc resonances.

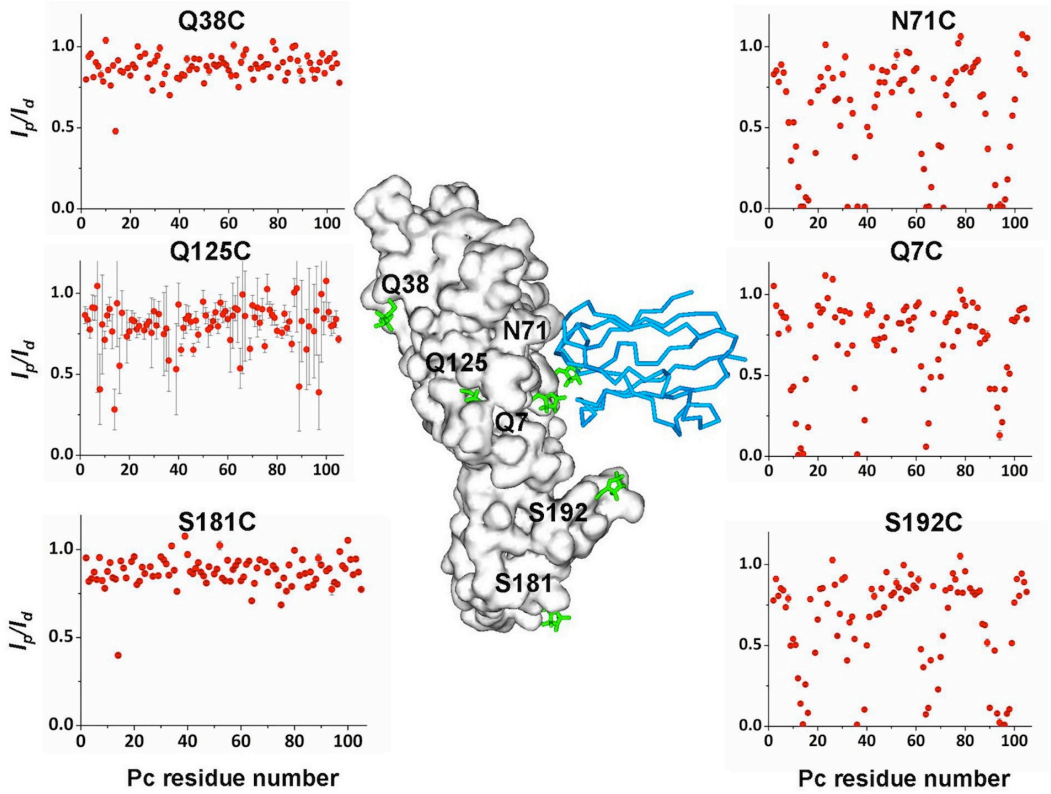

Figure 4.4. PRE in the $^{N\text{-}Ph}$complex. *Central panel*. Location of the spin labels (green sticks) modelled on the ^{N}Cyt *f* (PDB entry 2ZT9). Cyt *f* is shown as grey surface and Pc is represented as cyan C_α trace, oriented as the PCS-based final complex. *Side panels*. The I_p/I_d ratios are plotted versus the Pc residue number for each of the spin label positions on Cyt *f*. The error bars represent the uncertainty for I_p/I_d ratios based on the noise levels of the spectra. For most points, the error bar is within the symbol.

It is noteworthy that also spin labels attached on the backside of Cyt *f*, at the positions Q38 and Q125, or located far away, S181, showed a moderate to large decrease for some resonances. The large error bars calculated for the ratios in the presence of Q125C mutant are due to the lower concentration of Pc in this sample (45 μM) as compared to the other mutants (100 μM) resulting in a low signal-to-noise ratio. The I_p/I_d ratios were used to determine the PRE (Γ_2). In the fast exchange regime (see above) the observed PREs are weighted averages of free Pc, encounter complex and final complex. The PREs were extrapolated to the 100% bound state (encounter complex + final complex) by dividing by the fraction of bound Pc. The PREs caused by each spin label were mapped on the surface of Pc (Figure 4.5).

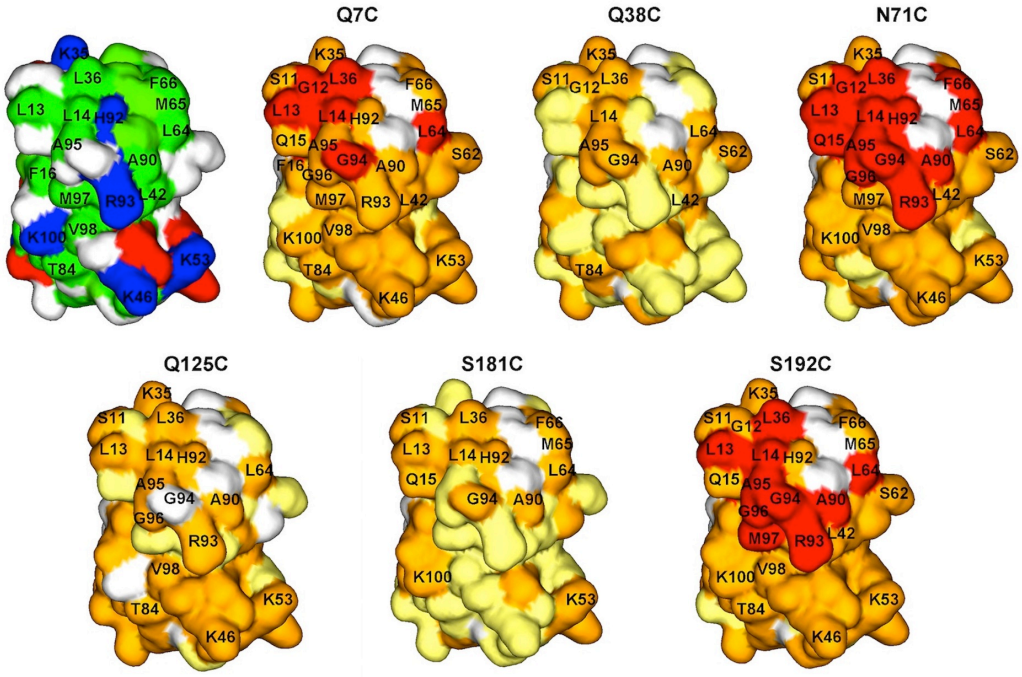

Figure 4.5. PRE maps of ^{15}N enriched-Zn substituted ^{Ph}Pc in the presence of MTSL-conjugated ^{N}Cyt *f*, color-coded on a surface model of Pc (PDB-entry 2Q5B). Experimental PREs were extrapolated to 100% bound Pc. Residues with $\Gamma_2 \geq 200$ s^{-1} are colored in red; with 10 s^{-1}< Γ_2< 200 s^{-1} in orange and with $\Gamma_2 \leq 10$ s^{-1} in light yellow. Prolines and residues with overlapping resonances are colored in white. On the top left, Pc is colored according to its charge distribution. Negatively and positively charged residues are shown in red and blue, respectively. Hydrophobic residues are in green and polar residues in white.

Even though the three spin labels located at the same side of Cyt *f* as the binding site (Q7C, N71C, S192C) are relatively far from each other, the PRE patterns are very similar and resemble the CSP map in the presence of wild type Cyt *f* (Figure 4.1B). The qualitative similarity of the PRE patterns suggests that Pc samples a large area of the Cyt *f* surface, while maintaining the same relative orientation to Cyt *f*. The highest PREs were observed for residues located in the hydrophobic patch of Pc, indicated as main binding site in the PCS-based final complex. Most of these residues are hydrophobic or polar, with the exception of R93 that was strongly affected by PRE in the presence of spin labels in N71 and S192. The same residue exhibited a high CSP in the presence of wild type Cyt *f* (Figure 4.1B). Interestingly, for most of these residues moderate PREs were also observed in the presence of spin labels attached to the backside of Cyt *f* with respect to the PCS-based binding site of Pc, indicating that Pc also visits this part of Cyt *f*.

The encounter complex was visualized by ensemble docking. This approach is based on the fact that PREs result from the weighted average contribution of all species in solution, which are either in the final or in the encounter orientations.[84] To represent all species that contribute to the observed PREs, multiple conformers of a protein are simultaneously docked on the other protein to obtain a population distribution that fits the experimental data. For the calculations the PREs are converted into distances and used as restraints for the docking. Each

docking yields a unique ensemble of orientations that account for the experimental PREs. The ensemble docking of ^{Ph}Pc and ^{N}Cyt *f* was essentially performed as described for the $^{N\text{-}N}$complex in Chapter III and the size of the ensemble was set to *N*=7, where *N* represents the number of copies of Pc in the ensemble. To separate the PRE contribution of the complex in the final state, the averaged back calculated PREs from the PCS-based models of the final complex were subtracted from experimental PREs and the resulting PREs were converted into distance restraints. A series of ensemble docking calculations was then carried out by varying the population of the final state (f_2) from 1-0. The resulting ensembles were evaluated by calculating the average distance violation over all experimental distances. The average distance violations were plotted versus the percentage of the encounter complex (Figure 4.6).

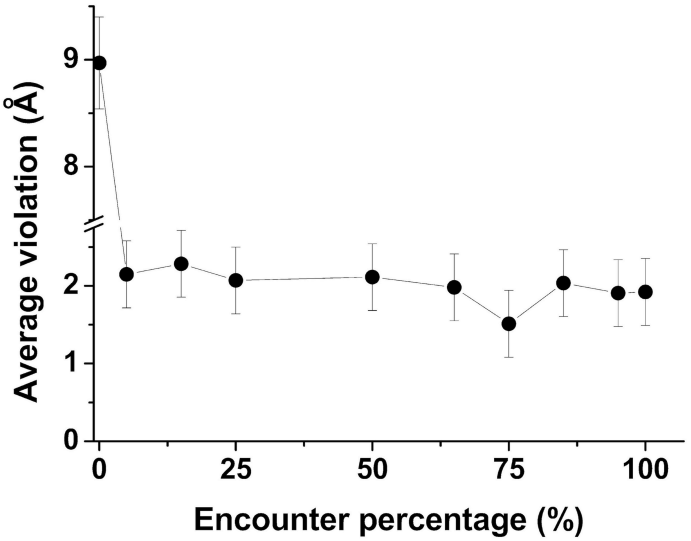

Figure 4.6. Plot of the average violation of all experimental distances versus the ensemble percentage included in the restraints for the calculations. Error bars represent 2 × SD of the average violations obtained from three independent calculations performed with N= 7 and f_2= 0.

The violations show that the observed PREs are not explained by the PCS-based structure alone. A significant decrease in the average violation is already observed when the encounter complex is taken to be 5%. Further increase of the encounter complex fraction in the restraints did not improve the fit of the data. For all generated ensembles an average violation of about 2 Å was observed.
The calculations for the representation of the encounter complex were performed assuming a pure encounter state (f_1=1). The comparison of the back calculated distances between the oxygen atom of the spin labels and the amide protons of all Pc conformers of the generated encounter complex (red line in Figure 4.7) and the back calculated distances in the PCS-based models of the final complex (blue line) shows that only the generated encounter complex fits the experimental PRE data (green dots and line).

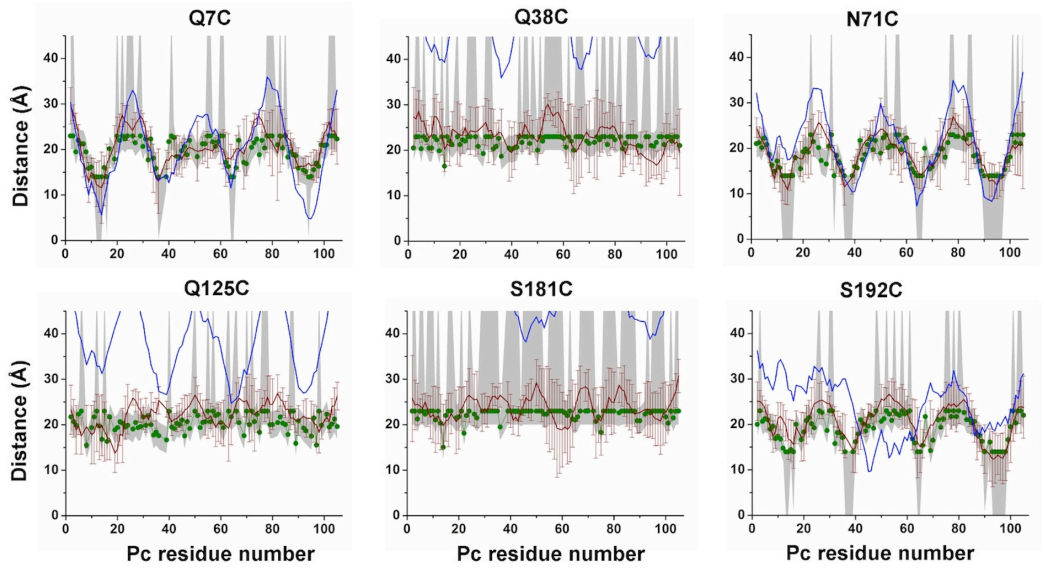

Figure 4.7. Ensemble docking. Experimental and back calculated average distances between Pc amide protons and oxygen atoms of MTSL conjugated to Cyt *f* are plotted against the Pc residue number. The green circles and lines represent the experimental distances and the grey areas indicate the error margins. The average distances back calculated from the 20 lowest-energy solutions of the PRE driven ensemble docking are shown as a red line with error bars representing the SD. The average back calculated distances from the PCS-based final complex models are shown as a blue line. Calculations were performed with $N = 7$ and $f_1 = 1$.

The main deviation is represented by S192, indicating that ^{Ph}Pc spends more time close to this spin label than expected from the PCS-based models. This suggests that PREs from S192 mainly arise from the encounter complex. Most of calculated distances from the generated encounter complex lie within the error margins of the experimental values. Deviations were observed for the spin label Q125C, likely due to the poor data quality (see above). Since in principle both PCS and PRE report on intra-complex dynamics, the PCSs from Cyt *f* iron to amide backbone protons of Pc were back calculated for the ensemble generated using PRE (PCS^{ens}). To determine the population fractions of the complex in the final and in the encounter states PCS^{ens} were linearly combined with the calculated PCSs (PCS^{final}) from the final models using different population fractions of the encounter complex (see Experimental Section, Equation 4.6). The different combinations were correlated to the experimental PCSs by means of a Q factor (Equation 4.4). To account for the uncertainty of the size of the axial component of the magnetic susceptibility anisotropy of Cyt *f* Fe^{III}, a range of $\Delta\chi_{ax}$ values was used for the determination of the Q values. In Figure 4.8, the Q factors are plotted versus the percentage of the encounter complex. As illustrated also in Chapter III, the fit the data depends on the size of $\Delta\chi_{ax}$ and a reliable estimation of the fraction of the encounter complex unfortunately cannot be made.

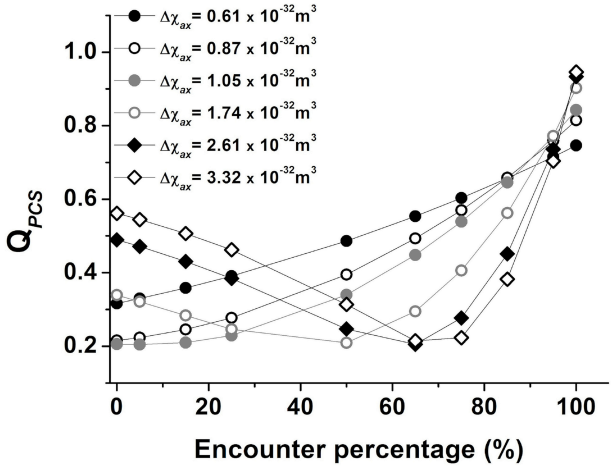

Figure 4.8. Q factors calculated for a combination of experimental PCSs measured for the specific complex and for different combination of back calculated PCSs from the final and the encounter complex. Q factors are plotted versus the percentage of the encounter complex. The Q factors were calculated at different values of the size of the axial component of the magnetic susceptibility tensor (see Experimental Section).

To represent the encounter complex, an ensemble from 145 docking solutions with *N*=7 and f_1=1, with a total of 1015 Pc conformers was generated (Figure 4.9A).

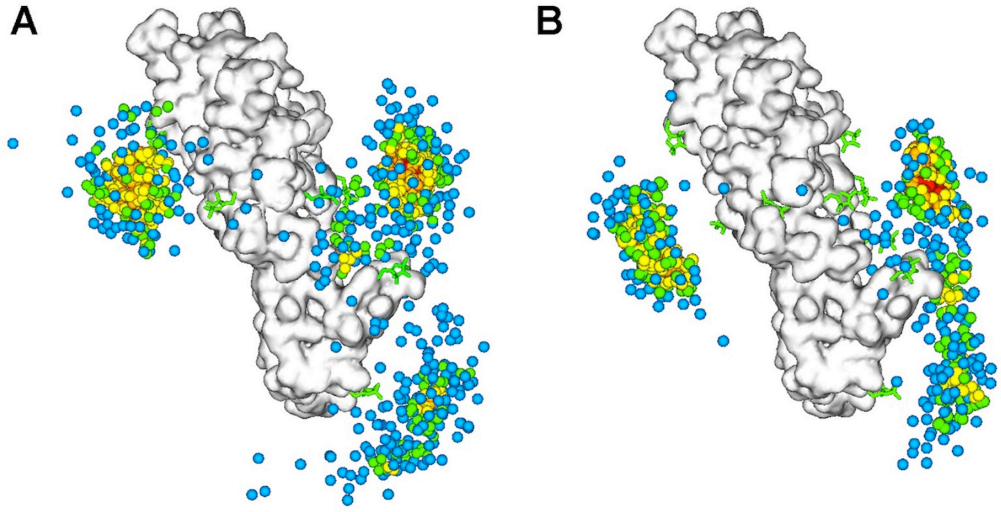

Figure 4.9. Comparison of the encounter complexes of $^{N\text{-}Ph}$complex (A) and $^{N\text{-}N}$complex (B). ^{N}Cyt *f* is shown as a white surface and spin labels as green sticks. Pc CoMs are represented by spheres, color-coded to indicate the density of the distributions, decreasing from red to blue. Densities were determined by counting the number of neighbours within 2.5 Å.

The centers-of-mass (CoMs) of Pc were colored according to the density of distribution, with red and blue representing the largest and smallest density, respectively. It should be noted that the incomplete coverage of spin labels on Cyt *f* surface implies that also other Cyt *f* surface areas could be involved in the encounter complex. The current analysis shows that the encounter complex is at least distributed over three extensive areas of Cyt *f* surface. All three encounters showed high density in the central regions and low density at the edge of the

encounter complex. The most extended area is located in the vicinity of the binding site found in the final complex models, the second is in front of the small domain of Cyt *f* and the third on the backside relative to the final complex. The third area is an artifact due to the use of the soluble part of ^{N}Cyt *f*. *In vivo*, Cyt *f* is embedded on the thylakoid membrane that will prevent Pc from binding on this side (Chapter III). In all three areas the interface comprises large patches of polar and hydrophobic residues. Despite the fact that in this study a less extensive portion of the Cyt *f* surface was monitored, the encounter complex resembles the one found for the $^{N\text{-}N}$complex (Figure 4.9B). The encounter ensemble of $^{N\text{-}Ph}$complex is more extensive and covers a larger area of the hydrophobic regions of Cyt *f*. In $^{N\text{-}N}$complex, stronger charge interactions may lead to more defined encounter regions. In the $^{N\text{-}N}$complex one continuous diffusive encounter region is present on the side of the binding site, while in the $^{N\text{-}Ph}$complex two distinct diffusive areas can be seen. To evaluate the distribution of the ET active complexes, the CoMs of ^{Ph}Pc are colored according the calculated distance between Cu in Pc and Fe in Cyt *f*, with red and blue representing the smallest and largest distance, respectively (Figure 4.10A). Like for the $^{N\text{-}N}$complex (Figure 4.10B), the encounter complex orientations compatible with rapid ET (red dots, Cu-Fe distance ≤ 16 Å) are located only in front of the haem, in the close vicinity of the binding site found in the final complex.

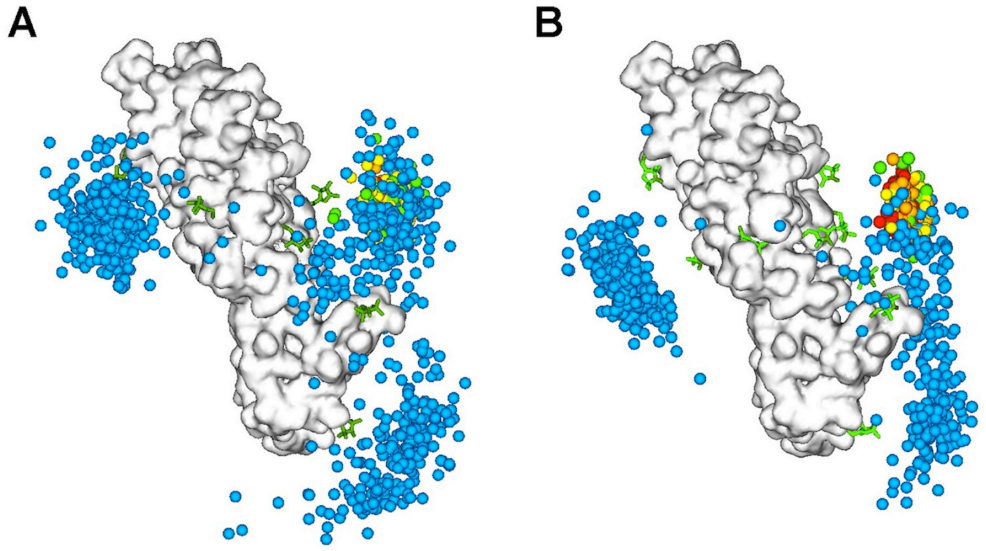

Figure 4.10. Comparison of the encounter complexes of $^{N\text{-}Ph}$complex (A) and $^{N\text{-}N}$complex (B). Cyt *f* is shown as a white surface and spin labels as green sticks. Pc CoMs are represented by spheres. Pc CoMs are color-coded to indicate the distance between Cu in Pc and Fe in Cyt *f*, increasing from red to blue (red ≤ 16 Å; orange ≤ 18 Å; yellow ≤ 20 Å; green ≤ 22 Å; blue > 22 Å).

Role of electrostatic interactions in complex formation

The effect of ionic strength (*I*) on the binding shifts of ^{Ph}Pc in the presence of reduced ^{N}Cyf *f* at Cyf *f*:Pc molar ratio 3:1 was investigated at NaCl concentrations of 100 mM (*I*= 110 mM) and 200 mM (*I*= 210 mM). The CSPs ($\Delta\delta_H$)

were defined relative to the control measurements recorded on free ^{Ph}Pc at the same ionic strenth values. The $\Delta\delta_H$ at the different salt concentrations were plotted versus ^{Ph}Pc residue numbers (Figure 4.11A).

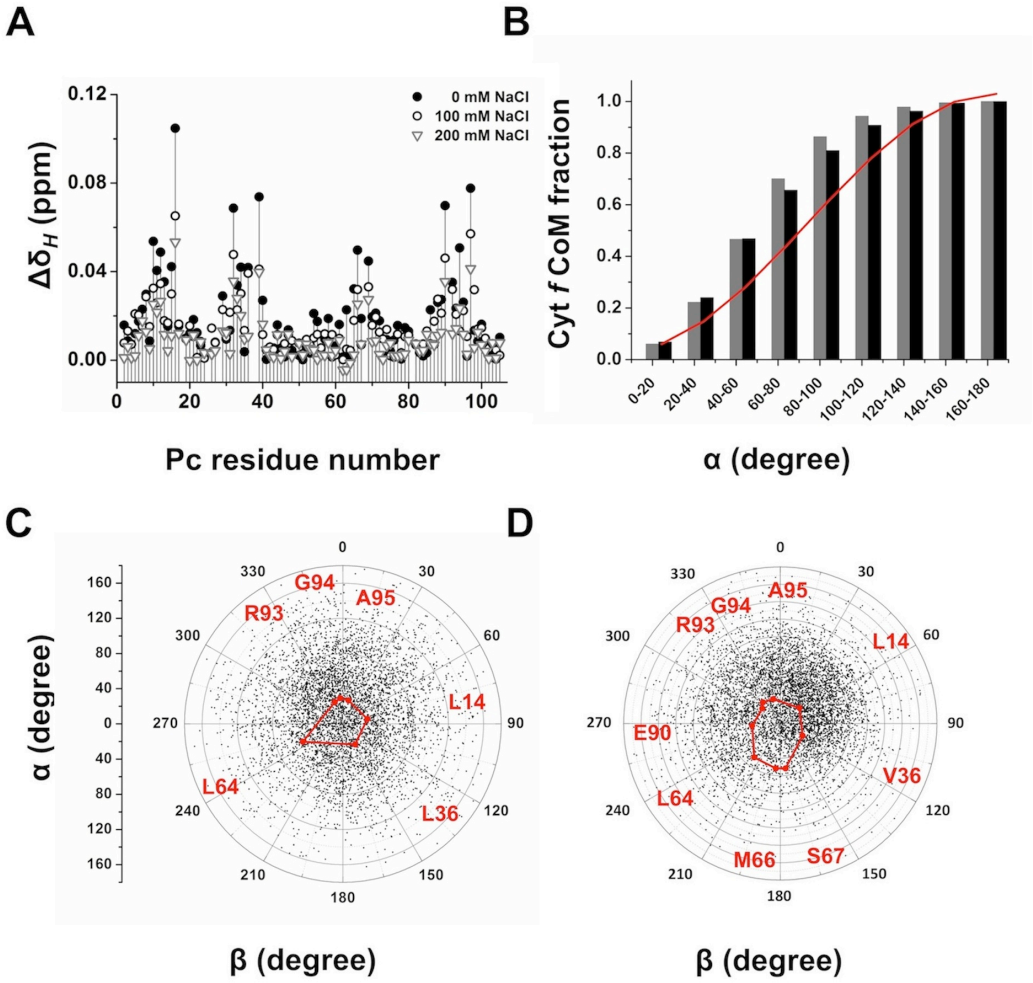

Figure 4.11. Role of electrostatic interactions in Cyt *f*-Pc complexes. A) Ionic strength dependence of $\Delta\delta_H$ for ^{Ph}Pc backbone amide protons in the presence of reduced ^{N}Cyt *f* at *I*= 10 mM (black dots), *I*= 110 mM (black circles) and *I*= 210 mM (grey triangles). (B, C, D) Analysis of the encounter complex generated by MC simulations. B) The cumulative fraction of Cyt *f* CoMs for the α angle is plotted for the $^{N\text{-}Ph}$complex (black bars) and $^{N\text{-}N}$complex (grey bars). The red line represents the cumulative fraction for a completely random distribution around a sphere. Plots of the position of the ^{N}Cyt *f* CoMs with respect to ^{Ph}Pc (C) and ^{N}Pc (D), in the MC ensembles. The red line connects the positions of hydrophobic patch residues. The Nε of H92 is at the center of the plots in panels C and D.

In rigid-body MC simulations the association of two proteins is simulated on the basis of their electrostatic potentials.[57] On the assumption that the formation of the encounter complex is purely driven by long-range electrostatic forces,[21] PRE and MC simulations were successfully combined for the visualization of the encounter complex of cytochrome *c* and cytochrome *c* peroxidase, demonstrating that the formation of this complex could be explained by

electrostatic interactions alone.[28] The same approach on the $^{N\text{-}N}$complex revealed to be inadequate to describe the encounter complex, which appears to be stabilized by electrostatic as well as hydrophobic interactions (Chapter III). At the same time, MC simulations provided evidence of the electrostatic preorientation of Pc towards Cyt *f*, as was found on the basis of CSP and PRE data. MC simulations were performed for the $^{N\text{-}Ph}$complex to establish whether electrostatic preorientation of ^{Ph}Pc can occur despite the negative charge of both proteins. The calculations produced an ensemble consisting of the Boltzmann distribution of orientations of Cyt *f* around Pc. An ensemble of 5000 structures was randomly selected from the entire set of two million solutions and the positions of Cyt *f* CoMs were plotted in Figure 4.11C. The position in the plot is determined by two angles. The first is the cone angle (α) formed by the Cyt *f* CoM, the Pc CoM and the Nε atom of copper ligand H92, taken as the center of the hydrophobic patch. The larger this angle is, the further the Cyt *f* CoM is rotated away from the hydrophobic patch. The α angle is represented by the circles in Figure 4.11C and 4.11D. The second angle, β, indicates the position on the cone, and represents the side of Pc to which the Cyt *f* CoM is rotated. The hydrophobic patch is delineated by a red line marked with residue numbers. Figure 4.11C shows that Cyt *f* binds in a diffusive manner, but toward the hydrophobic patch side of ^{Ph}Pc thantoward the other end. Clearly, preorientation occurs due to electrostatic interactions. This finding is also illustrated in Figure 4.11D. The cumulative fraction of Cyt *f* CoMs for the α angle is plotted (black bars). The red line represents the cumulative fraction for a completely random distribution around a sphere. The fraction of CoMs with α angles of less than 90° is larger than 50%, so more than half of the CoMs is present around the half of Pc that comprises the hydrophobic patch, due to electrostatic preorientation. This suggests that despite the net negative charge of ^{Ph}Pc, the localization of positive charges promotes the formation of and oriented complex. For comparison, the same calculations, on the basis of an earlier study (Chapter III) are shown for the $^{N\text{-}N}$complex in Figure 4.11B (grey bars) and 4.11D. For this complex, the preorientation is stronger and shows a more defined binding spot for α = 60°-80° and β = 30°-120°. The primary reason for this difference between the complexes of ^{N}Cyt *f* with ^{N}Pc and ^{Ph}Pc is the presence of two Lys residues (K11 and K20) in this region of ^{N}Pc, which are substituted by serine and asparagine, respectively, in ^{Ph}Pc.

To compare the importance of ionic strength on the formation of the different Cyt *f*-Pc complexes, MC simulations were performed for $^{N\text{-}N}$complex, $^{N\text{-}Ph}$complex and $^{Ph\text{-}Ph}$complex at ionic strength values of 10 mM, 110 mM and 210 mM (Figure 4.12A-C). In the cases of $^{N\text{-}Ph}$complex (Figure 4.12B) and $^{Ph\text{-}Ph}$complex (Figure 4.12C), very sparsely distributed encounter complexes were observed at higher values of *I*. For the $^{N\text{-}N}$complex (Figure 4.12A), though the increase in ionic strength resulted in the production of more diffusive encounters, in which the Cyt *f* distribution covers a wider area of Pc surface than observed at low ionic strength, a preferable docking area could be still recognized and related to the diverse electrostatic properties of ^{N}Pc. The histograms of the electrostatic interaction energies show that at an ionic strength of 210 mM (green bars), the $^{N\text{-}Ph}$complex (Figure 4.12B) and $^{Ph\text{-}Ph}$complex (Figure 4.12C) have lost all electrostatic attraction. For the $^{N\text{-}N}$complex (Figure 4.12A) it is strongly reduced but not completely zero.

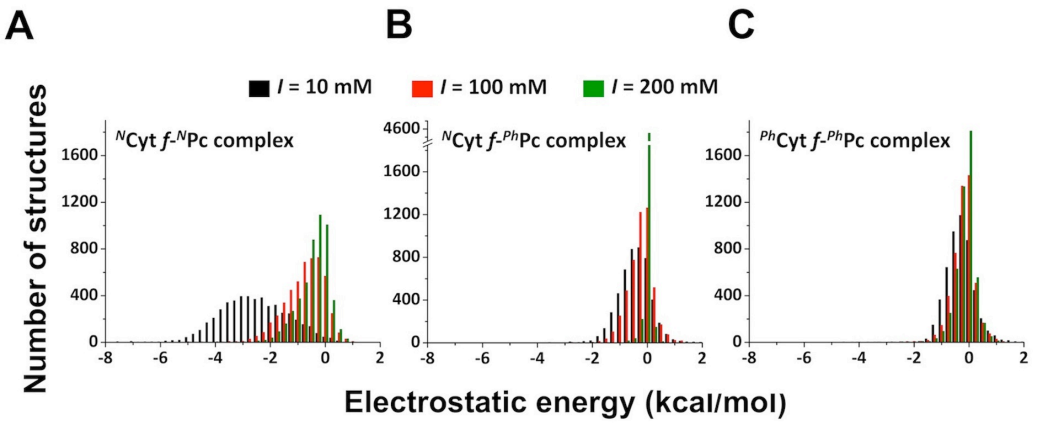

Figure 4.12. Electrostatic interaction histograms from MC simulation. MC simulations were performed at *I*= 10mM (black bars), *I*= 110mM (red bars) and *I*= 210mM (green bars) versus the electrostatic energy values for $^{N\text{-}N}$complexes (A), $^{N\text{-}Ph}$complexes (B) and $^{Ph\text{-}Ph}$complexes (C).

Comparison among Cyt *f*-Pc complexes

Recently, we proposed a model for the formation of the $^{N\text{-}N}$complex on the basis of the available kinetic and NMR data. Upon approach of the proteins, ^{N}Pc is rotated by electrostatic interactions to face ^{N}Cyt *f* with its hydrophobic patch leading to the formation of the encounter complex. This state is not stabilized only by charge interactions. Also hydrophobic interactions are important, allowing a smooth transition from encounter to ET-capable orientations by gradual increase of the hydrophobic overlap and sliding over the hydrophobic interface. It is interesting to interpret the data for the $^{N\text{-}Ph}$complex in the light of this model.
The most important difference between ^{N}Pc and ^{Ph}Pc is the net positive and negative charge, respectively. Given the highly negative charge on ^{N}Cyt *f* a poor interaction with ^{Ph}Pc is expected, if charge interactions are dominant. It was found that the affinity is five-fold lower for ^{Ph}Pc, suggesting that charges indeed play a role. This is also supported by the MC calculations that show less preorientation for ^{Ph}Pc than for ^{N}Pc. Nevertheless, some preorientation is still observed, indicating that the dipolar nature charge distribution is important in complex formation. The MC results are supported by the CSP and PCS data, which clearly demonstrate that the hydrophobic patch is the side of ^{Ph}Pc that is in contact with ^{N}Cyt *f*. However, the MC results do not agree quantitatively with the PRE data, indicating that electrostatic interactions alone are not sufficient to describe the encounter ensemble and the final complex.
The PCS based final complex shows predominantly hydrophobic contacts and the ^{Ph}Pc orientation is different from that in the $^{N\text{-}N}$complex, which can be explained by the substitution of several Lys residues on ^{Ph}Pc, resulting in the absence of several charge-charge interactions with negative residues on ^{N}Cyt f. The encounter complex produced using PRE driven ensemble docking is similar to that of the $^{N\text{-}N}$complex, though even more diffusive. In both encounter

complexes, Pc is found in contact with the non-polar surfaces of Cyt *f*, strongly suggesting that hydrophobic interactions indeed contribute to the encounter complex.

The PCS are much smaller in the $^{N\text{-}Ph}$complex than in the $^{N\text{-}N}$complex, suggesting that the encounter complex is more populated. The size of PCS strongly depends on the distance between the haem iron and the Pc nucleus that experiences the PCS. Thus, it is expected that in the encounter complex, which is spread over a large surface area of Cyt *f*, the PCS will be smaller than in the final complex. Orientation averaging may reduce the PCS further. The size of the PCS is about three-fold less for ^{Ph}Pc than for ^{N}Pc (Figure 4.3B).

In encounter complexes that are of an electrostatic nature CSPs are very small, compared to those in the final complex,[30,72] and increasing the fraction of the encounter complex strongly reduces the average size of the CSP in those complexes.[31] In complex with ^{N}Cyt *f* the CSPs for ^{Ph}Pc are also reduced compared to ^{N}Pc (Figure 4.1C, 4.1D) but not very much, much less than three-fold. This is an interesting observation because significant CSPs may be expected also in the encounter complex, if it is stabilized by hydrophobic contacts. The chemical shift of amide groups is particular sensitive to polarity and hydrogen bond formation, so the desolvation of the protein surface that accompanies the formation of hydrophobic contacts is expected to cause significant CSPs.

It is interesting to compare the effects of ionic strength in the $^{N\text{-}N}$complex, $^{N\text{-}Ph}$complex and $^{Ph\text{-}Ph}$complex. Addition of 200 mM NaCl to the $^{Ph\text{-}Ph}$complex (*I*= 210 mM) had essentially no effect on the fraction of bound Pc,[54] suggesting that hydrophobic contacts strongly dominate the interaction. The K_D was difficult to determine accurately and was reported to be about 1 mM. Here, we use a range of 1-3 mM. If it is assumed that the hydrophobic contribution to the binding is similar in the three complexes, the contribution of the electrostatic interactions can be estimated for the $^{N\text{-}N}$complex and the $^{N\text{-}Ph}$complex. An affinity of 1-3 mM equals a change in free energy of binding of 4.1 – 3.4 kcal/mol. The K_D values for the $^{N\text{-}N}$complex and the $^{N\text{-}Ph}$complex are 80[29] and 400 μM in the absence of salt (*I* = 10 mM), suggesting an additional contribution from the charge interactions of 1.5 – 2.2 kcal/mol and 0.55 – 1.2 kcal/mol, respectively. Thus, the electrostatic interaction represents 27%-38% and 12%-26% of the total binding energy in the $^{N\text{-}N}$complex and the $^{N\text{-}Ph}$complex.

Addition of 160 mM NaCl (*I* = 170 mM) to the $^{N\text{-}N}$complex reduced the fraction bound by about 50%[49] and it can be calculated on the basis of the protein concentrations used in that experiment that the binding energy decreased with 1.6 kcal/mol, nearly abolishing the charge-charge contribution. The same is observed for the $^{N\text{-}Ph}$complex, where addition of 200 mM NaCl (*I* = 210 mM) reduces the fraction bound by 60%, which translates to a loss of -0.8 kcal/mol of binding energy under the given experimental conditions. Thus, under the assumption that the hydrophobic contribution is conserved among these complexes, it can be concluded that the electrostatic contribution represents one-third of the binding energy for the $^{N\text{-}N}$complex at low ionic strength and much less at more physiological values. For the $^{N\text{-}Ph}$complex this fraction is even smaller. The trend is qualitatively supported by the electrostatic interaction histograms from the MC calculations (Figure 4.12A-C). This is an important finding in relation to earlier *in vivo* studies, in which no significant effects of mutation of charged

residues in the interface of an algal Cyt *f*-Pc complex could be detected in activity assay.[63-64] These result suggest that charge interactions are not relevant for the complex. On the other hand, the results on the cross-complex show that even weak electrostatic interactions are effective in pre-orientation Pc to face Cyt *f* with its hydrophobic patch. Furthermore, many charged residues on both proteins are conserved, especially among plants, suggesting that at least under some circumstances the charge interactions contribute significantly to the electron transfer process in photosynthesis.

In conclusion, the current study fully supports the model complex formation described for the $^{N\text{-}N}$complex. In $^{N\text{-}Ph}$complex the role of charges has not been abolished, but it is reduced in favor of hydrophobic contacts, creating a complex with biophysical properties that is a mixture of the $^{N\text{-}N}$complex and the $^{Ph\text{-}Ph}$complex. The variation that is observed between mechanisms of complex formation observed for the same complex from different species, shows that several ways exist to achieve both fast ET and rapid turn-over in protein complexes. The common denominator may be a low affinity and low energy barriers between the subsequent states in the reaction.